

All-solid-state Batteries

High-Entropy Lithium Argyrodite Solid Electrolytes Enabling Stable All-Solid-State Batteries

Shenghao Li⁺, Jing Lin⁺, Mareen Schaller, Sylvio Indris, Xin Zhang, Torsten Brezesinski, Ce-Wen Nan, Shuo Wang,* and Florian Strauss*

Abstract: Superionic solid electrolytes (SEs) are essential for bulk-type solid-state battery (SSB) applications. Multicomponent SEs are recently attracting attention for their favorable charge-transport properties, however a thorough understanding of how configurational entropy (ΔS_{conf}) affects ionic conductivity is lacking. Here, we successfully synthesized a series of halogen-rich lithium argyrodites with the general formula $\text{Li}_{5.5}\text{PS}_{4.5}\text{Cl}_x\text{Br}_{1.5-x}$ ($0 \leq x \leq 1.5$). Using neutron powder diffraction and ^{31}P magic-angle spinning nuclear magnetic resonance spectroscopy, the $\text{S}^{2-}/\text{Cl}^-/\text{Br}^-$ occupancy on the anion sublattice was quantitatively analyzed. We show that disorder positively affects Li-ion dynamics, leading to a room-temperature ionic conductivity of 22.7 mS cm^{-1} (9.6 mS cm^{-1} in cold-pressed state) for $\text{Li}_{5.5}\text{PS}_{4.5}\text{Cl}_{0.8}\text{Br}_{0.7}$ ($\Delta S_{\text{conf}} = 1.98R$). To the best of our knowledge, this is the first experimental evidence that configurational entropy of the anion sublattice correlates with ion mobility. Our results indicate the possibility of improving ionic conductivity in ceramic ion conductors by tailoring the degree of compositional complexity. Moreover, the $\text{Li}_{5.5}\text{PS}_{4.5}\text{Cl}_{0.8}\text{Br}_{0.7}$ SE allowed for stable cycling of single-crystal $\text{LiNi}_{0.9}\text{Co}_{0.06}\text{Mn}_{0.04}\text{O}_2$ (s-NCM90) composite cathodes in SSB cells, emphasizing that dual-substituted lithium argyrodites hold great promise in enabling high-performance electrochemical energy storage.

Introduction

All-inorganic solid-state batteries (SSBs) are regarded as a possibility to boost energy and power density of rechargeable Li batteries. To achieve this, solid electrolyte (SE) materials with a high ionic conductivity, good (electro)chemical stability and some mechanical softness (for processing reasons) are needed.^[1–3] And indeed, the ongoing quest for advanced SEs has led to the discovery of ceramic materials, either crystalline or amorphous, that show conductivities exceeding those of liquid (organic) electrolytes.^[4,5] These highly conducting materials are solely sulfide based, which in turn is favorable for maintaining good contact with the other electrode constituents, as they are relatively soft.^[6–10] However, their (electro)chemical stability window is narrow,^[11–14] and therefore an artificial interface is typically required to avoid direct contact with the cathode and/or anode material (to allow for reversible SSB operation).^[15–18]

Some highly conducting SEs reported in the literature are, unfortunately, of limited practical relevance, as they contain scarce elements,^[19–23] thus the continuing need for further exploration of novel conductors made from more abundant materials. In this regard, lithium argyrodites, originally reported for $\text{Li}_6\text{PS}_5\text{X}$ with $\text{X}=\text{Cl}, \text{Br}, \text{I}$, have emerged as an important class of materials.^[24–26] To increase the ionic conductivity in this structure type, the phosphorus, sulfur and halide sites have been substituted with other elements and, in some cases, room-temperature conductivities beyond 10 mS cm^{-1} were achieved.^[20,22,27] This increase

[*] S. Li,⁺ X. Zhang, S. Wang
 Center of Smart Materials and Devices, State Key Laboratory of Advanced Technology for Materials Synthesis and Processing & School of Material Science and Engineering, Wuhan University of Technology
 Wuhan 430070 (China)
 E-mail: shuowang@whut.edu.cn

J. Lin,⁺ T. Brezesinski, F. Strauss
 Institute of Nanotechnology, Karlsruhe Institute of Technology (KIT)
 Hermann-von-Helmholtz-Platz 1, 76344 Eggenstein-Leopoldshafen (Germany)
 E-mail: florian.strauss@kit.edu

M. Schaller, S. Indris
 Institute for Applied Materials-Energy Storage Systems (IAM-ESS), Karlsruhe Institute of Technology (KIT)
 Hermann-von-Helmholtz-Platz 1, 76344 Eggenstein-Leopoldshafen (Germany)

C.-W. Nan
 State Key Laboratory of New Ceramics and Fine Processing, School of Materials Science and Engineering, Tsinghua University
 Beijing 100084 (China)
 S. Wang
 Foshan (Southern China) Institute for New Materials
 Foshan 528200 (China)

[⁺] These authors contributed equally to this work.

© 2023 The Authors. Angewandte Chemie International Edition published by Wiley-VCH GmbH. This is an open access article under the terms of the Creative Commons Attribution License, which permits use, distribution and reproduction in any medium, provided the original work is properly cited.

in ionic conductivity by about an order of magnitude is usually a result of an altered Li sublattice (presence of additional Li sites, shortened Li⁺-Li⁺ jump distances, etc.) and an increased S²⁻/X⁻ site disorder, both of which leads to facile lithium diffusion. Another approach to boost ionic conductivity in lithium argyrodites is the substitution of sulfur with a halogen (Cl⁻ or Br⁻), leading to an increase in Li vacancies and more pronounced S²⁻/X⁻ site disorder. Recently, such halogen-rich, lithium-deficient argyrodites (e.g., Li_{5.5}PS_{4.5}Cl_{1.5}) are attracting interest, as they not only possess a high ionic conductivity but also show a better (electro)chemical stability than the parent Li₆PS₅Cl.^[28-34] It has also been shown that a second halogen can be introduced, and with that, the conductivity further improves.^[35-37] From a structural perspective, it has been recognized that anion disorder induced by halogen mixing and varying the halogen content can have a profound effect on ionic conductivity.^[29,35,36,38-41]

Introducing a large anion and/or cation disorder into the host lattice of polyanionic SE materials, referring to high-entropy ion conductors, has been garnering a lot of attention lately, due to potential improvements in conductivity and (electro)chemical stability.^[21,42-47] In principle, high-entropy materials (HEMs) refer to materials with a shared occupation of several different elements on a single crystallographic site. This increases the configurational entropy (ΔS_{conf}),^[48-50] and can either lead to the emergence of new and/or improved properties or help stabilize metastable phases through the entropy contribution to the Gibbs energy of the multicomponent phase.^[51-53] HEMs are usually referred to as having a $\Delta S_{\text{conf}} > 1.5R$. In recent years, various HEMs have been synthesized, including oxides, sulfides and carbides, and employed as electrode materials in batteries, catalysts and as dielectric capacitors, among others.^[54-56] However, only a few examples of high-entropy Li-ion conductors adopting different structures and being suitable for application in batteries have been reported so far.^[21,42,45,46] Regarding lithium argyrodites, recently, a multicationic substituted HEM, Li_{6.5}[P_{0.25}Si_{0.25}Sb_{0.25}Ge_{0.25}]S₅I, showing an ionic conductivity of $> 10 \text{ mS cm}^{-1}$ at room temperature, along with a very low activation energy for lithium diffusion of 0.20 eV, has been reported. However, the correlation between the degree of disorder and the ionic conductivity remains unclear.

To shed light on this, we prepared a series of (dual-substituted) halogen-rich lithium argyrodite samples with a total halogen content of 1.5 moles and systematically varied the Cl⁻ to Br⁻ ratio in Li_{5.5}PS_{4.5}Cl_xBr_{1.5-x} (with $x = 0, 0.2, 0.4, 0.6, 0.8, 1.0, 1.2$ and 1.5). Their crystal structure was probed using a combination of neutron powder diffraction (NPD) and ³¹P magic-angle spinning (MAS) nuclear magnetic resonance (NMR) spectroscopy, indicating that a maximum anion-disordered sublattice is achieved with Li_{5.5}PS_{4.5}Cl_{0.8}Br_{0.7}. Using complementary electrochemical impedance spectroscopy (EIS) and ⁷Li pulsed field gradient (PFG) NMR measurements, it is shown that this particular material also possesses the highest ionic conductivity among all prepared samples. Overall, we demonstrate, to our knowledge for the first time, that there is a direct correlation

between ΔS_{conf} and ionic conductivity in this class of ion conductors. Finally, the Li_{5.5}PS_{4.5}Cl_{0.8}Br_{0.7} SE was also tested in pellet-type SSB cells and found to allow for stable cycling over 700 cycles.

Results and Discussion

To understand the impact of halogen substitution on the charge-transport properties, eight samples with varying composition were synthesized. An initial structural assessment using laboratory X-ray diffraction (XRD) revealed their phase purity, with the patterns showing a gradual shift of the reflections to higher 2θ values with increasing bromine content (see Figure S1a and b). Le Bail analysis further indicated that the patterns can be indexed to the $F\bar{4}3m$ space group and showed, as expected, a linear decrease in the a lattice parameter (and therefore unit cell volume) with increasing chlorine content (see Figure S1c), confirming solid-solution behavior over the whole compositional range. This is due to the smaller ionic radius of Cl⁻ compared to Br⁻,^[57] as the nominal sulfur, phosphorus and lithium contents remain unchanged. The calculated lattice parameters are given in Table S1. Because XRD is not able to differentiate between chlorine and sulfur, due to very similar X-ray scattering cross sections, and neither provides insight into the Li substructure, high-resolution NPD data were collected at room temperature from selected samples, namely Li_{5.5}PS_{4.5}Cl_xBr_{1.5-x} with $x = 0, 0.4, 0.8, 1.2$ and 1.5 . A representative diffraction pattern for Li_{5.5}PS_{4.5}Cl_{0.8}Br_{0.7}, along with the corresponding Rietveld plot, is presented in Figure 1a. Note that the lattice parameters derived from XRD and NPD are in good agreement (see Figure S1c). The calculated crystal structure is shown in Figure 1b, with the “free” S²⁻ and halogen ions forming a face-centered cubic anion sublattice (Wyckoff positions $4a$ and $4d$) and additional S²⁻ ions being located in half of the tetrahedral voids ($16e$) around the octahedral sites ($4b$), thereby forming [PS₄]³⁻ tetrahedra. Moreover, in the argyrodite structure, S²⁻ ($4d$) and halogen anions ($4a$) are known to mix over the respective Wyckoff positions, referring to anion site inversion. Comparable ionic radii of the respective anions (e.g., S²⁻ and Cl⁻) or structural distortions usually enable a high level of halogen anions occupying the $4d$ Wyckoff position, i.e., high sulfur/halogen site inversion. As mentioned previously, Rietveld analysis of the NPD data enabled us to quantify the shared S²⁻/Cl⁻/Br⁻ occupancy on both the $4a$ and $4d$ sites. The results are shown in Figure 1c and d. For Li_{5.5}PS_{4.5}Br_{1.5} ($x = 0$), the $4a$ and $4d$ sites were found to be occupied by 89% and 61% bromine, respectively. If the bromine is gradually replaced by chlorine, the overall halogen occupancy on $4a$ decreases (see Figure 1c), while that on the $4d$ site increases (see Figure 1d). This, for instance, leads to a chlorine occupancy of 63% and 90% on the $4a$ and $4d$ Wyckoff positions, respectively, for Li_{5.5}PS_{4.5}Cl_{1.5} ($x = 1.5$), in agreement with literature data.^[28] Moreover, for the mixed chlorine/bromine-containing samples (i.e., Li_{5.5}PS_{4.5}Cl_xBr_{1.5-x} with $x = 0.4, 0.8$ and 1.2), bromine apparently prefers to be situated on $4a$, whereas chlorine

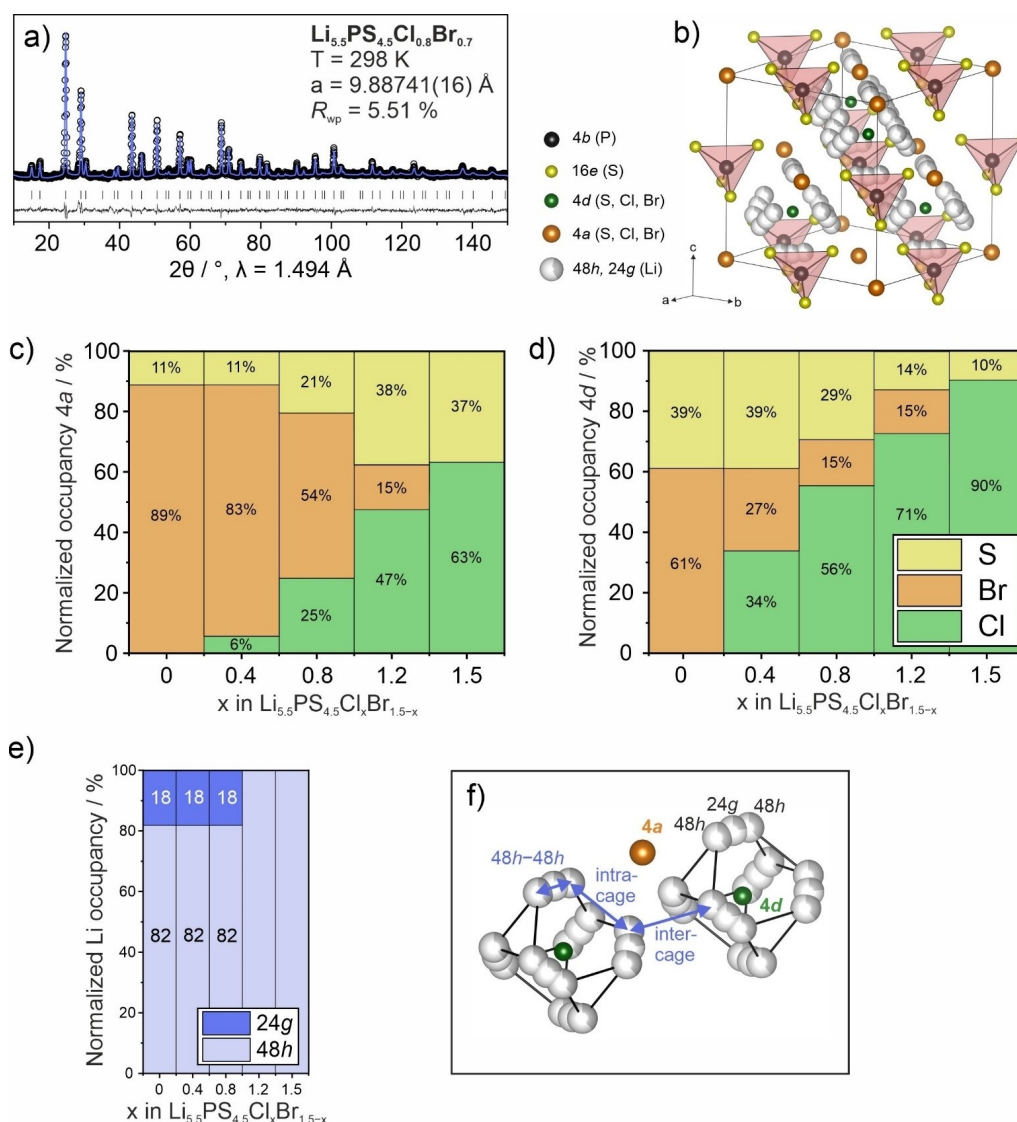


Figure 1. Structural characterization of the halogen-substituted lithium argyrodite solid electrolytes. (a) NPD pattern and corresponding Rietveld analysis for $\text{Li}_{5.5}\text{PS}_{4.5}\text{Cl}_{0.8}\text{Br}_{0.7}$ and (b) schematic view of the crystal structure with the different Wyckoff positions and elemental constituents indicated in the legend to the left. Refined structural parameters and compositions are given in Tables S2–S8. The normalized occupancies of the 4a and 4d Wyckoff positions are depicted in panels (c) and (d). (e) Normalized Li occupancies and (f) two neighboring Li cages with the 4a and 4d nearest positions being indicated.

predominantly occupies the 4d site. This leads to a decrease in average ionic radius with increasing chlorine content (see Figure S2a).

The halogen distribution in the crystal structure also affects the Li sublattice. In particular, two occupied Li positions, namely 48h and 24g, were identified for $\text{Li}_{5.5}\text{PS}_{4.5}\text{Cl}_x\text{Br}_{1.5-x}$ with $x=0, 0.4$ and 0.8 , showing a similar distribution with 18% for 24g and 82% for 48h (see Figure 1e). Interestingly, we found that when the 4a and 4d Wyckoff positions share a similar average ionic radius (see Figure S2a), only one of the Li positions (48h) is occupied. This difference in Li distribution depending on the anion composition is also, at least in part, affected by the average ionic charge. As can be seen from Figure S2b, the average ionic charge on the 4d site decreases with increasing chlorine

content, eventually leading to a single occupied Li position for $x=1.2$ and 1.5 . Thus, depending on the average ionic radius and charge of the shared crystallographic positions, lithium seems to be forced into occupying either only one or two sites (different Coulomb interactions). In the substructure, three different Li^+-Li^+ jump distances are of relevance (see Figure 1f). The 48h–48h doublet (through the nominal 24g transition site) and intracage jumps occur within the Li cages surrounding the halogen/sulfur-mixed 4d position. However, the inter-cage jumps are those that are believed to strongly determine the long-range transport properties, and the neighboring 4a position may strongly affect these relatively large Li^+-Li^+ distances.^[22,41] However, we find that the different jump distances are similar for the

$\text{Li}_{5.5}\text{PS}_{4.5}\text{Cl}_x\text{Br}_{1.5-x}$ samples employed in this work (see Figure 1f and Table S7).

After having revealed distinct differences in the average crystal structure (long-range ordering), the local structure of the samples was probed using ^6Li and ^{31}P MAS NMR spectroscopy. First of all, a gradual shift of the peak intensity maxima in the ^6Li MAS NMR spectra, from 1.23 to 1.0 ppm, with increasing chlorine content is found (see Figure 2a). This can be explained by the withdrawing of electron density from lithium with increasing Cl^- occupancy (decreasing S^{2-} level) on the $4d$ site (located within the Li cages, see Figure 1f). In addition, for $\text{Li}_{5.5}\text{PS}_{4.5}\text{Cl}_x\text{Br}_{1.5-x}$ with $x=0, 0.4$ and 0.8 , the presence of a distinct shoulder peak of relatively lower intensity is evident at higher chemical shifts. This

indicates the presence of two different Li positions, in agreement with the results from NPD analysis (see Figure 1e). It should be noted that the chemical shifts observed for the endmembers $\text{Li}_{5.5}\text{PS}_{4.5}\text{Cl}_{1.5}$ and $\text{Li}_{5.5}\text{PS}_{4.5}\text{Br}_{1.5}$ agree well with those reported in the literature.^[28,37] From the ^{31}P MAS NMR measurements, complex spectra showing multiple contributions were obtained. However, they also revealed a gradual shift from higher to lower chemical shift (see Figure 2b). While $\text{Li}_{5.5}\text{PS}_{4.5}\text{Cl}_{1.5}$ shows multiple contributions around 83 ppm, the peaks are centered around 92 ppm for $\text{Li}_{5.5}\text{PS}_{4.5}\text{Br}_{1.5}$. This is in agreement with the ^{31}P MAS NMR shifts seen for $\text{Li}_6\text{PS}_5\text{X}$ ($\text{X}=\text{Cl}$ or Br).^[24] Unlike $\text{Li}_{5.5}\text{PS}_{4.5}\text{Cl}_{1.5}$, for which two major peaks and a broad shoulder at higher chemical shift were detected,

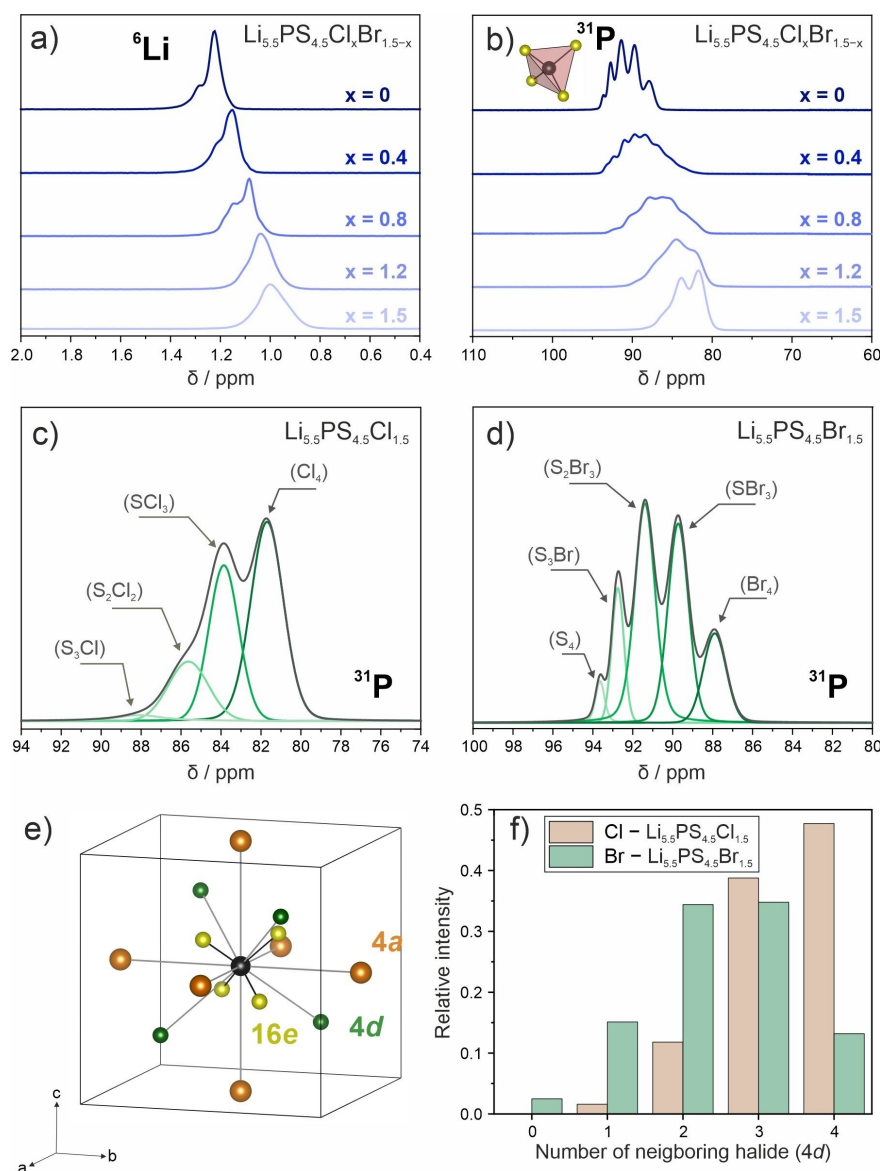


Figure 2. Local structure of the halogen-substituted lithium argyrodite solid electrolytes. (a) ^6Li and (b) ^{31}P MAS NMR spectra. Curve fits to the ^{31}P data for (c) $\text{Li}_{5.5}\text{PS}_{4.5}\text{Cl}_{1.5}$ and (d) $\text{Li}_{5.5}\text{PS}_{4.5}\text{Br}_{1.5}$ showing the different contributions. (e) Nearest neighbors around the $[\text{PS}_4]^{3-}$ tetrahedra with phosphorus and sulfur atoms shown in black and yellow, respectively. (f) Calculated probability of specific chemical environments around P from fitting a binomial distribution to the relative intensities in the ^{31}P MAS NMR spectra.

$\text{Li}_{5.5}\text{PS}_{4.5}\text{Br}_{1.5}$ exhibits five peaks of different intensities. For the mixed chlorine/bromine-containing samples, again broad ^{31}P MAS NMR spectra were obtained, with the peak intensities being blurred, indicating a larger degree of disorder. This was to be expected given that three different elements are now sharing the $4d$ site. To reveal the specific chemical environment of the two endmembers, the spectra were curve fitted (see Figure 2c and d). As shown in Figure 2c, the four different contributions for $\text{Li}_{5.5}\text{PS}_{4.5}\text{Cl}_{1.5}$ pertain to the number of nearest neighboring chlorine/sulfur atoms around the $[\text{PS}_4]^{3-}$ tetrahedra on the $4d$ Wyckoff position (see Figure 2e). The composition ranges from four chlorine atoms (Cl_4 with highest intensity contribution) to a mixed environment consisting of three sulfur and one chlorine atom (S_3Cl with lowest intensity contribution). A purely sulfur-containing environment (S_4) was not observed for $\text{Li}_{5.5}\text{PS}_{4.5}\text{Cl}_{1.5}$. In contrast, for $\text{Li}_{5.5}\text{PS}_{4.5}\text{Br}_{1.5}$, all possible configurations can be identified (see Figure 2d). Results from quantitative analysis of the different environments, i.e., relative peak intensities, are shown in Figure 2f. Unlike $\text{Li}_{5.5}\text{PS}_{4.5}\text{Cl}_{1.5}$, where a pure chlorine environment is most probable, a mixed $\text{S}^{2-}/\text{Br}^-$ distribution over the neighboring sites is preferred in the case of $\text{Li}_{5.5}\text{PS}_{4.5}\text{Br}_{1.5}$.

The relative peak intensities observed in the ^{31}P MAS NMR spectra for $\text{Li}_{5.5}\text{PS}_{4.5}\text{Cl}_{1.5}$ and $\text{Li}_{5.5}\text{PS}_{4.5}\text{Br}_{1.5}$ can be well described by a simple binomial distribution:

$$p(n) = \frac{4!}{n! \cdot (4-n)!} \cdot q^n \cdot (1-q)^{4-n} \quad (1)$$

with n being the number of halogen ions on the four neighboring $4d$ sites around the $[\text{PS}_4]^{3-}$ tetrahedra and q representing the overall fraction of halogen ions occupying these sites. Fitting such a binomial distribution to the relative intensities (see Figure 2f), $q=0.83$ for $\text{Li}_{5.5}\text{PS}_{4.5}\text{Cl}_{1.5}$ ($x=1.5$) and $q=0.60$ for $\text{Li}_{5.5}\text{PS}_{4.5}\text{Br}_{1.5}$ ($x=0$) were obtained. These values are in excellent agreement with the occupancies determined by NPD (see Figure 2d). A similar analysis for the samples containing both halogen elements is challenging, as assignments of the different contributions to mixed $\text{S}^{2-}/\text{Cl}^-/\text{Br}^-$ environments (15 different possible compositions on the four neighboring $4d$ sites) requires the description by a multinomial distribution.

Next, the charge-transport properties were examined via complementary EIS and ^7Li PFG NMR spectroscopy. EIS measurements were conducted between 10 and 60 °C on cold-pressed pellets for all samples. At 25 °C, only a capacitive tail was visible (see Figure S3), indicating high ionic conductivity. Fitting of the spectra revealed ionic conductivities ranging from 4.2 to 9.6 mS cm^{-1} for $\text{Li}_{5.5}\text{PS}_{4.5}\text{Br}_{1.5}$ (lowest) and $\text{Li}_{5.5}\text{PS}_{4.5}\text{Cl}_{0.8}\text{Br}_{0.7}$ (highest), respectively. The corresponding results can be found in Table S9. From Arrhenius fitting of the temperature-dependent conductivity (see Figure 3a), the activation energies (E_A) were calculated to be in the range between 0.30 and 0.34 eV (see Table S9).

The lithium diffusion coefficient (D_{Li}) was probed using ^7Li PFG NMR spectroscopy at temperatures from 29 to 65 °C for the $\text{Li}_{5.5}\text{PS}_{4.5}\text{Cl}_x\text{Br}_{1.5-x}$ samples with $x=0, 0.4, 0.8,$

1.2 and 1.5. The echo damping versus gradient field strength is shown in Figure S4 and revealed only a single contribution for all materials. From the measurements, the D_{Li} at 29 °C was determined to be in the range of $1.0\text{--}1.4 \times 10^{-11} \text{ m}^2 \text{ s}^{-1}$ (see Figure 3b). These values are among the highest observed for Li-ion conductors^[28,58] and suggest an extremely fast mobility, in line with the conductivity deduced from the cold-pressed pellets via EIS. With increasing the temperature to 65 °C, the $\text{Li}_{5.5}\text{PS}_{4.5}\text{Cl}_{0.8}\text{Br}_{0.7}$ sample exhibits the strongest increase in D_{Li} , reaching $4.8 \times 10^{-11} \text{ m}^2 \text{ s}^{-1}$. From Arrhenius fitting of the temperature-dependent D_{Li} data (see Figure 3c), the activation energies were calculated, lying between 0.24 eV for $\text{Li}_{5.5}\text{PS}_{4.5}\text{Br}_{1.5}$ and 0.32 eV for $\text{Li}_{5.5}\text{PS}_{4.5}\text{Cl}_{1.2}\text{Br}_{0.3}$. Overall, they are in a similar range as those determined by EIS and about 0.1 eV higher compared to other superionic lithium argyrodites.^[20,22,23,37,45] Using the Nernst-Einstein equation, the room-temperature conductivities were calculated from the diffusion coefficients. The obtained values are very high, reaching 22.7 mS cm^{-1} for $\text{Li}_{5.5}\text{PS}_{4.5}\text{Cl}_{0.8}\text{Br}_{0.7}$. So far, very few thiophosphate-based Li-ion conductors with a room-temperature conductivity above 20 mS cm^{-1} have been reported, crystallizing either in the argyrodite or LGPS structure type.^[21,34,35,59] Finally, the conductivities and activation energies from EIS were compared to those calculated from the ^7Li PFG NMR data (see Table S9). As can be seen from Figure 3d, the ionic conductivities determined by EIS are lower by about 10 mS cm^{-1} , however they exhibit a similar trend with composition. This means that the pure bromine-containing endmember possesses the lowest ionic conductivity among all samples. If chlorine is introduced into the structure, the conductivity increases up to $x=0.8$, thereafter a slight decrease is observed. Note that the gap between the conductivity values from the two techniques is most likely rooted in poor grain boundary contacts, as ^7Li PFG NMR spectroscopy examines the bulk ionic conductivity, whereas EIS probes the overall sample conductivity (cold-pressed pellets). Thus, the measured diffusion coefficient ($\approx 10^{-11} \text{ m}^2 \text{ s}^{-1}$ at 29 °C) corresponds to a Li displacement of about 1.3 μm within the diffusion time scale (30 ms).^[60] This is much smaller than the average particle size of these solid electrolytes, as observed by scanning electron microscopy (SEM) imaging and elemental mapping (see Figure S5a–e), supporting our assumption that solely bulk ionic conductivity is probed in the ^7Li PFG NMR spectroscopy measurements. Moreover, EIS was conducted on the $\text{Li}_{5.5}\text{PS}_{4.5}\text{Cl}_{0.8}\text{Br}_{0.7}$ sample that was hot-pressed into a dense pellet (see Supporting Information for details). The room-temperature ionic conductivity of the sintered pellet was determined to be about 19.8 mS cm^{-1} (see Figure S6), which agrees with the ^7Li PFG NMR results (absence of grain-boundary resistance). Regarding E_A , first a decrease with increasing chlorine content up to $x=0.8$ is observed, followed by a slight increase, reaching the lowest value for the best-conducting sample $\text{Li}_{5.5}\text{PS}_{4.5}\text{Cl}_{0.8}\text{Br}_{0.7}$. This is in contrast to the E_A determined by ^7Li PFG NMR spectroscopy, showing a gradual increase with increasing chlorine content. Again, the slightly different trends are due to poor

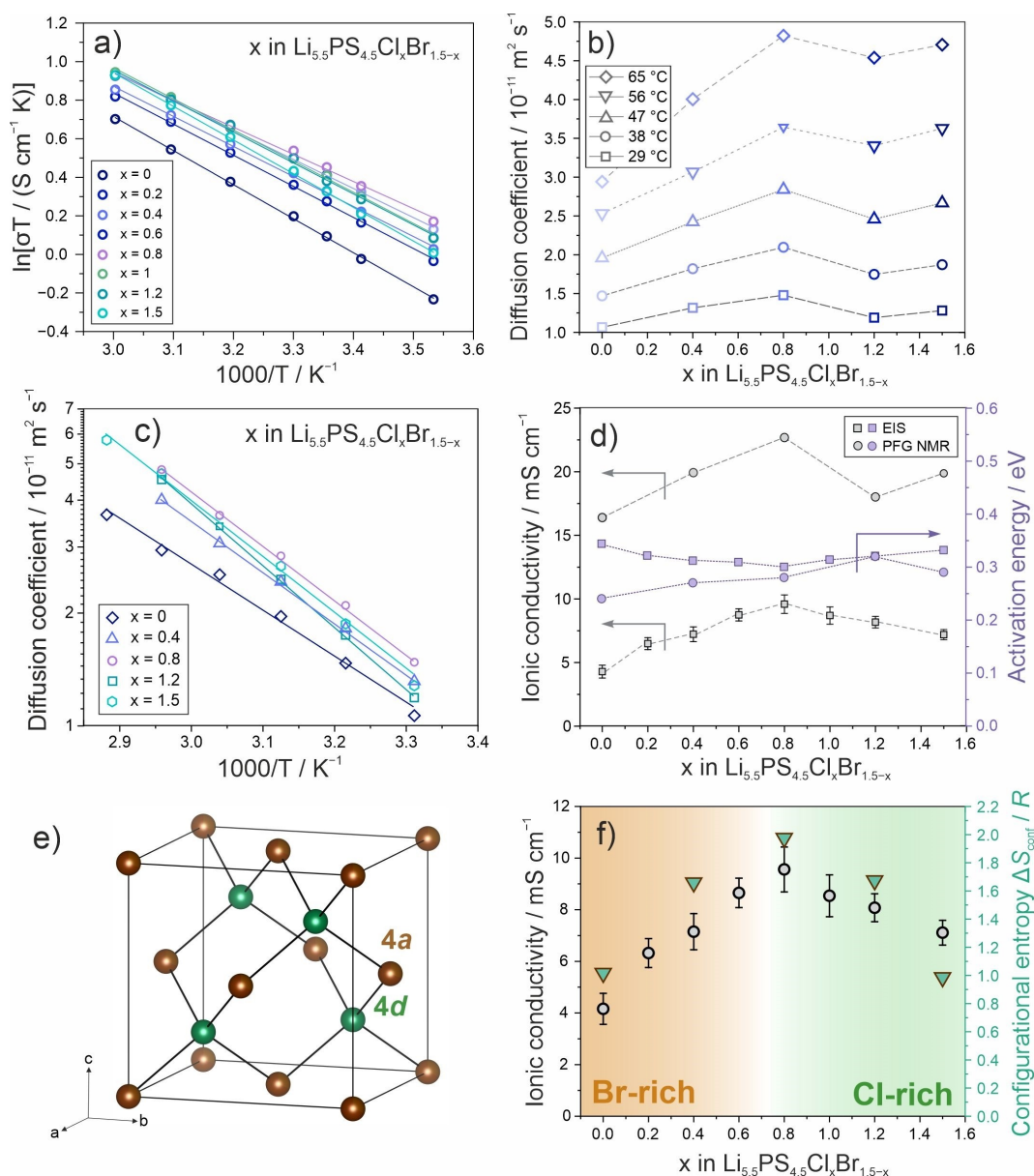


Figure 3. Charge-transport properties of the $\text{Li}_{5.5}\text{PS}_{4.5}\text{Cl}_x\text{Br}_{1.5-x}$ samples. (a) Arrhenius plots of conductivity (EIS). (b) Lithium diffusion coefficients at different temperatures and (c) corresponding Arrhenius plots (^7Li PFG NMR). (d) Ionic conductivities and activation energies at room temperature determined by EIS and ^7Li PFG NMR spectroscopy. (e) Schematic representation of the anion sublattice, including the 4a and 4d Wyckoff sites. (f) Correlation between configurational entropy calculated from the specific occupancies of the anion sublattice shown in panel (e) and ionic conductivity. If no error bars are visible, the standard deviation is smaller than the symbol.

grain-boundary contacts in the cold-pressed samples used for the EIS measurements.

On the basis of the above data, structure–property relationships can be established. In this regard, it is important to recall that recent reports have shown a possible beneficial effect of structural disorder in the rigid host lattice (framework) on ion diffusion of the mobile species (Li^+ , Na^+ , H^+).^[42–45,61,62] In the case of the $\text{Li}_{5.5}\text{PS}_{4.5}\text{Cl}_x\text{Br}_{1.5-x}$ samples, the ΔS_{conf} refers to the number of possibilities for distributing sulfur, chlorine and bromine ions in the zincblende-type anion sublattice (4a and 4d Wyckoff positions) within the argyrodite structure (see Figure 3e).

Usually, a mixing of elements over these two crystallographic sites has been expressed as halogen/sulfur site-inversion or disorder. However, if more than one halogen element is introduced, this descriptor is not accurate anymore. To express the halogen/sulfur disorder more precisely, the ΔS_{conf} presents a much better descriptor, as it also takes into account the partial occupancies of the different elemental constituents (not only mixing over two crystallographic sites). This means that if a high ΔS_{conf} is calculated, the number of anion conformations is large, comparable to the number of conformations a complex organic molecule can adopt. In other words, configurational entropy is a

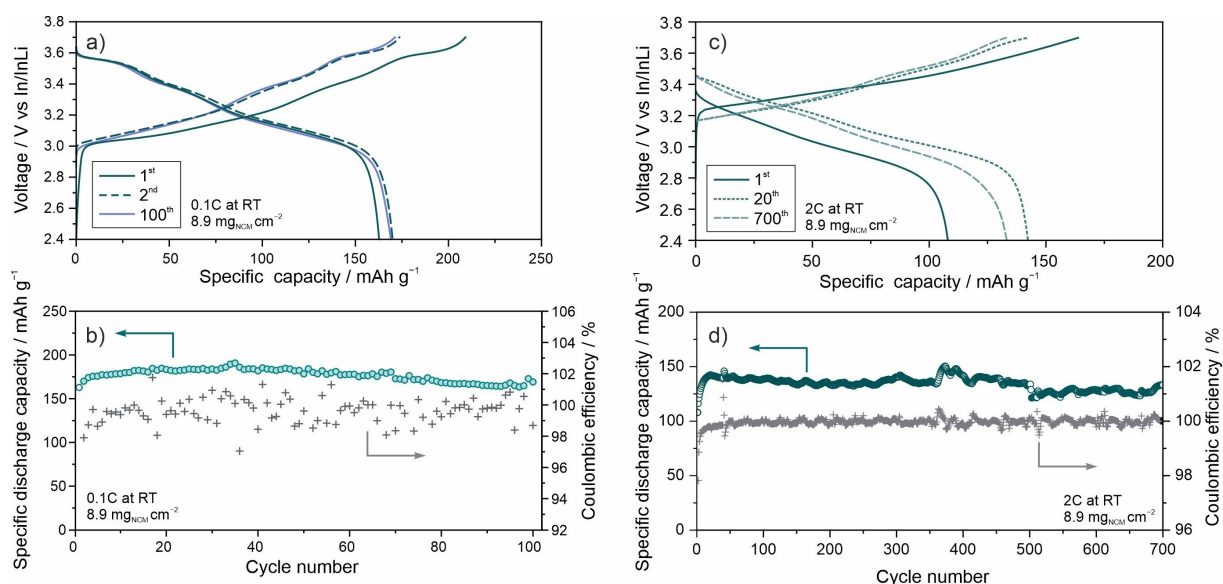


Figure 4. Electrochemical cycling of SSB cells with $\text{Li}_{5.5}\text{PS}_{4.5}\text{Cl}_{0.8}\text{Br}_{0.7}$ as SE. (a) Voltage profiles for the 1st, 2nd and 100th cycles at 0.1 C rate and (b) corresponding capacity retention and Coulomb efficiencies. (c) Voltage profiles for the 1st, 20th and 700th cycles at 2 C rate and (d) corresponding capacity retention and Coulomb efficiencies.

measure of anion disorder: The more equally the three anions are distributed over the two available crystallographic sites, the higher the ΔS_{conf} is. This in turn leads to local structural distortions (on the unit cell level, see Figure S2). Therefore, a high ΔS_{conf} of the anion sublattice leads to a statistical uncertainty for lithium diffusion pathways, i.e., broadened (Li-site) energy distributions and facilitated ion motion through the structure. If the ΔS_{conf} is calculated from the specific site occupancies determined by NPD, we find a maximum for the $\text{Li}_{5.5}\text{PS}_{4.5}\text{Cl}_{0.8}\text{Br}_{0.7}$ sample, which also exhibits the highest ionic conductivity (see Figure 3f). This result confirms that disorder of the anion sublattice is responsible for increased ionic conductivity. We assume that the structural complexity increases the vibrational entropy (phonon behavior), which is also known to affect ion diffusion through so-called phonon-ion interaction.^[63] For example, Ding et al. recently investigated lattice softening in argyrodite $\text{Li}_6\text{PS}_5\text{Cl}$ and found that the low-energy phonon modes (<10 meV) associated with Li are also important for realizing fast ion transport.^[64] Taking into account the large disorder of the anion sublattice in $\text{Li}_{5.5}\text{PS}_{4.5}\text{Cl}_{0.8}\text{Br}_{0.7}$, phonon effects cannot be ignored and might be responsible, at least to some degree, for the improved Li-ion conductivity.

Finally, the material exhibiting the highest ionic conductivity ($\text{Li}_{5.5}\text{PS}_{4.5}\text{Cl}_{0.8}\text{Br}_{0.7}$) was tested as SE in pellet-stack SSB cells using a borate-coated, single-crystalline layered Ni-rich oxide cathode ($\text{s-NCM90@Li}_3\text{BO}_3$, 8.9 mg cm^{-2} loading) and an In/InLi anode. First, they were cycled at room temperature and at a rate of 0.1 C. In the initial cycle, specific charge and discharge capacities of 209 and 163 mAh g^{-1} were achieved, corresponding to a Coulomb efficiency (CE) of $\approx 78\%$ (see Figure 4a). Subsequently, both capacity and CE increased slightly, followed by relatively stable cycling over 100 cycles (see Figure 4b). In

the 100th cycle, the cells delivered a specific discharge capacity of 169 mAh g^{-1} . During long-term cycling, the CE fluctuated between 98 and 100%, suggesting minor detrimental side reactions. To further assess the performance of the $\text{Li}_{5.5}\text{PS}_{4.5}\text{Cl}_{0.8}\text{Br}_{0.7}$ SE, the SSB cells were electrochemically tested at a higher C-rate. Specifically, they were subjected to cycling at 2 C. In the initial cycle, specific charge and discharge capacities of 165 and 108 mAh g^{-1} were achieved (see Figure 4c). From the cycling data, the formation of a kinetically stable SE|s-NCM90@ Li_3BO_3 interface, preventing further SE degradation, seems likely. After the first cycle, the specific discharge capacity gradually increased, reaching 142 mAh g^{-1} in the 20th cycle. Also, the CE stabilized above 99.5% after five cycles. Minor capacity decay upon further cycling was observed, with 133 mAh g^{-1} in the 700th cycle (see Figure 4d). The performance assessment of the $\text{Li}_{5.5}\text{PS}_{4.5}\text{Cl}_{0.8}\text{Br}_{0.7}$ SE at both low and high C-rate provides evidence that dual-substituted, halogen-rich argyrodite SEs allow for stable SSB operation. We assume that the as-formed cathode interface/decomposition interphase exhibits a low partial electronic conductivity and kinetically prevents further degradation.^[65] This is corroborated by the limited reversibility on the first cycle, but high CE observed during long-term cycling.

Conclusion

In summary we have investigated the structure–property relationships in halogen-rich $\text{Li}_{5.5}\text{PS}_{4.5}\text{Cl}_x\text{Br}_{1.5-x}$ SE materials for the solid-solution range of $0 \leq x \leq 1.5$. Using a combination of high-resolution NPD and ^{31}P MAS NMR spectroscopy, we show that a certain anion occupation over the 4a and 4d Wyckoff sites occurs, which also affects the lithium substructure. Charge-transport characteristics were revealed

by combined temperature-dependent EIS and ^7Li PFG NMR spectroscopy measurements. Overall, we demonstrate that an increased $\text{S}^{2-}/\text{Cl}^-/\text{Br}^-$ disorder, which can be expressed in the form of configurational entropy, leads to very fast Li-ion dynamics. This is reflected in a lithium diffusion coefficient of $1.4 \times 10^{-11} \text{ m}^2 \text{ s}^{-1}$ (29°C), as well as in an ionic conductivity of 9.6 mS cm^{-1} in cold-pressed state and a bulk ionic conductivity of 22.7 mS cm^{-1} (25°C) determined by ^7Li PFG NMR spectroscopy. This remarkable achievement is made possible by using inexpensive precursors, making the material suitable for large-scale application. Overall, the results indicate that compositional disorder in the anion sublattice of lithium argyrodites directly facilitates ion diffusion, meaning the conductivity is increasing with increasing configurational entropy. In addition, the sample with the highest conductivity, $\text{Li}_{5.5}\text{PS}_{4.5}\text{Cl}_{0.8}\text{Br}_{0.7}$, was tested as SE in SSB cells and found to allow for stable cycling over 700 cycles (with virtually no capacity decay), indicating its suitability for industrial use. Therefore, the concept of increasing ionic conductivity by increasing configurational entropy might pave the way toward the development of advanced SEs, with halogen-rich lithium argyrodites emerging as a promising class of materials.

Acknowledgements

S.W. and C.W.N. acknowledge the Natural Science Foundation of China (grant no. 52388201 and 52302305). S.W. acknowledges the Natural Science Foundation of Hubei Province (grant no. 2022CFB760) and the Guangdong Basic and Applied Basic Research Foundation (grant no. 2021A1515110312). J.L. acknowledges the Fonds der Chemischen Industrie (FCI) for financial support. F.S. is grateful to the Federal Ministry of Education and Research (BMBF) for funding within the project MELLi (03XP0447). This research used resources at the Spallation Neutron Source (SNS), a DOE Office of Science User Facility operated by the Oak Ridge National Laboratory (ORNL). This work is based on experiments performed at the Swiss spallation neutron source SINQ, Paul Scherrer Institute (PSI), Villigen, Switzerland (proposal no. 20051234). The authors thank Xinxin Tan for providing the NCM90 cathode material and Dr. Denis Cheptiakov for assistance in the NPD measurements. Open Access funding enabled and organized by Projekt DEAL.

Conflict of Interest

The authors declare no conflict of interest.

Data Availability Statement

The data that support the findings of this study are available from the corresponding author upon reasonable request.

Keywords: Argyrodite • High-Entropy Materials • Solid Electrolyte • Solid-State Batteries

- [1] J. Janek, W. G. Zeier, *Nat. Energy* **2023**, *8*, 230–240.
- [2] A. L. Robinson, J. Janek, *MRS Bull.* **2014**, *39*, 1046–1047.
- [3] A. Bielefeld, D. A. Weber, J. Janek, *J. Phys. Chem. C* **2019**, *123*, 1626–1634.
- [4] J. Lau, R. H. DeBlock, D. M. Butts, D. S. Ashby, C. S. Choi, B. S. Dunn, *Adv. Energy Mater.* **2018**, *8*, 1800933.
- [5] Z. Zhang, Y. Shao, B. Lotsch, Y.-S. Hu, H. Li, J. Janek, L. F. Nazar, C.-W. Nan, J. Maier, M. Armand, *Energy Environ. Sci.* **2018**, *11*, 1945–1976.
- [6] R. Koerver, W. Zhang, L. de Biasi, S. Schweidler, A. O. Kondrakov, S. Kolling, T. Brezesinski, P. Hartmann, W. G. Zeier, J. Janek, *Energy Environ. Sci.* **2018**, *11*, 2142–2158.
- [7] Y. B. Song, H. Kwak, W. Cho, K. S. Kim, Y. S. Jung, K.-H. Park, *Curr. Opin. Solid State Mater. Sci.* **2022**, *26*, 100977.
- [8] J. A. Lewis, J. Tippens, F. J. Q. Cortes, M. T. McDowell, *Trends Chem.* **2019**, *1*, 845–857.
- [9] J. H. Teo, F. Strauss, F. Walther, Y. Ma, S. Payandeh, T. Scherer, M. Bianchini, J. Janek, T. Brezesinski, *Mater. Futures* **2022**, *1*, 015102.
- [10] J. Tippens, J. C. Miers, A. Afshar, J. A. Lewis, F. J. Q. Cortes, H. Qiao, T. S. Marchese, C. V. Di Leo, C. Saldana, M. T. McDowell, *ACS Energy Lett.* **2019**, *4*, 1475–1483.
- [11] J. Auvergniot, A. Cassel, J.-B. Ledeuil, V. Viallet, V. Seznec, R. Dedryvère, *Chem. Mater.* **2017**, *29*, 3883–3890.
- [12] R. Koerver, I. Aygün, T. Leichtweiß, C. Dietrich, W. Zhang, J. O. Binder, P. Hartmann, W. G. Zeier, J. Janek, *Chem. Mater.* **2017**, *29*, 5574–5582.
- [13] J. Auvergniot, A. Cassel, D. Foix, V. Viallet, V. Seznec, R. Dedryvère, *Solid State Ionics* **2017**, *300*, 78–85.
- [14] W. D. Richards, L. J. Miara, Y. Wang, J. C. Kim, G. Ceder, *Chem. Mater.* **2016**, *28*, 266–273.
- [15] S. P. Culver, R. Koerver, W. G. Zeier, J. Janek, *Adv. Energy Mater.* **2019**, *9*, 1900626.
- [16] A.-Y. Kim, F. Strauss, T. Bartsch, J. H. Teo, T. Hatsukade, A. Mazilkin, J. Janek, P. Hartmann, T. Brezesinski, *Chem. Mater.* **2019**, *31*, 9664–9672.
- [17] Y. Xiao, L. J. Miara, Y. Wang, G. Ceder, *Joule* **2019**, *3*, 1252–1275.
- [18] S. Wang, R. Fang, Y. Li, Y. Liu, C. Xin, F. H. Richter, C.-W. Nan, *J. Materiomics* **2021**, *7*, 209–218.
- [19] N. Kamaya, K. Homma, Y. Yamakawa, M. Hirayama, R. Kanno, M. Yonemura, T. Kamiyama, Y. Kato, S. Hama, K. Kawamoto, A. Mitsui, *Nat. Mater.* **2011**, *10*, 682–686.
- [20] L. Zhou, A. Assoud, Q. Zhang, X. Wu, L. F. Nazar, *J. Am. Chem. Soc.* **2019**, *141*, 19002–19013.
- [21] Y. Li, S. Song, H. Kim, K. Nomoto, H. Kim, X. Sun, S. Hori, K. Suzuki, N. Matsui, M. Hirayama, T. Mizoguchi, T. Saito, T. Kamiyama, R. Kanno, *Science* **2023**, *381*, 50–53.
- [22] M. A. Kraft, S. Ohno, T. Zinkevich, R. Koerver, S. P. Culver, T. Fuchs, A. Senyshyn, S. Indris, B. J. Morgan, W. G. Zeier, *J. Am. Chem. Soc.* **2018**, *140*, 16330–16339.
- [23] Y. Lee, J. Jeong, H. J. Lee, M. Kim, D. Han, H. Kim, J. M. Yuk, K.-W. Nam, K. Y. Chung, H.-G. Jung, S. Yu, *ACS Energy Lett.* **2022**, *7*, 171–179.
- [24] H.-J. Deiseroth, S.-T. Kong, H. Eckert, J. Vannahme, C. Reiner, T. Zaiß, M. Schlosser, *Angew. Chem. Int. Ed.* **2008**, *47*, 755–758.
- [25] S.-T. Kong, H.-J. Deiseroth, C. Reiner, Ö. Gün, E. Neumann, C. Ritter, D. Zahn, *Chem. Eur. J.* **2010**, *16*, 2198–2206.
- [26] S. Wang, Y. Zhang, X. Zhang, T. Liu, Y.-H. Lin, Y. Shen, L. Li, C.-W. Nan, *ACS Appl. Mater. Interfaces* **2018**, *10*, 42279–42285.

- [27] L. Zhou, N. Minafra, W. G. Zeier, L. F. Nazar, *Acc. Chem. Res.* **2021**, *54*, 2717–2728.
- [28] P. Adeli, J. D. Bazak, K. H. Park, I. Kochetkov, A. Huq, G. R. Goward, L. F. Nazar, *Angew. Chem. Int. Ed.* **2019**, *58*, 8681–8686.
- [29] S. Wang, W. Zhang, X. Chen, D. Das, R. Ruess, A. Gautam, F. Walther, S. Ohno, R. Koerver, Q. Zhang, W. G. Zeier, F. H. Richter, C.-W. Nan, J. Janek, *Adv. Energy Mater.* **2021**, *11*, 2100654.
- [30] T.-T. Zuo, F. Walther, J. H. Teo, R. Rueß, Y. Wang, M. Rohnke, D. Schröder, L. F. Nazar, J. Janek, *Angew. Chem. Int. Ed.* **2023**, *62*, e202213228.
- [31] L. Peng, C. Yu, S. Cheng, J. Xie, *Batteries & Supercaps* **2023**, *6*, e202200553.
- [32] W. D. Jung, J.-S. Kim, S. Choi, S. Kim, M. Jeon, H.-G. Jung, K. Y. Chung, J.-H. Lee, B.-K. Kim, J.-H. Lee, H. Kim, *Nano Lett.* **2020**, *20*, 2303–2309.
- [33] D. Gu, H. Kim, B.-K. Kim, J.-H. Lee, S. Park, *CrystEngComm* **2023**, *25*, 4182–4188.
- [34] H. Chen, Y. Lu, H. Zhang, Y. Zhou, J. Chen, X. Huang, B. Tian, *Chem. Commun.* **2023**, *59*, 7220–7223.
- [35] S. V. Patel, S. Banerjee, H. Liu, P. Wang, P.-H. Chien, X. Feng, J. Liu, S. P. Ong, Y.-Y. Hu, *Chem. Mater.* **2021**, *33*, 1435–1443.
- [36] S. Wang, X. Wu, Y. Liang, Y. Xu, S. Guan, K. Wen, X. Miao, Y. Liang, H. He, Y. Lin, Y. Shen, C.-W. Nan, *Front. Chem. Eng.* **2022**, *4*, 883502.
- [37] P. Wang, H. Liu, S. Patel, X. Feng, P.-H. Chien, Y. Wang, Y.-Y. Hu, *Chem. Mater.* **2020**, *32*, 3833–3840.
- [38] X. Feng, P.-H. Chien, Y. Wang, S. Patel, P. Wang, H. Liu, M. Immediato-Scuotto, Y.-Y. Hu, *Energy Storage Mater.* **2020**, *30*, 67–73.
- [39] S. Wang, A. Gautam, X. Wu, S. Li, X. Zhang, H. He, Y. Lin, Y. Shen, C.-W. Nan, *Adv. Energy Sustainability Res.* **2023**, *4*, 2200197.
- [40] M. A. Kraft, S. P. Culver, M. Calderon, F. Böcher, T. Krauskopf, A. Senyshyn, C. Dietrich, A. Zevalkink, J. Janek, W. G. Zeier, *J. Am. Chem. Soc.* **2017**, *139*, 10909–10918.
- [41] S. Ohno, B. Helm, T. Fuchs, G. Dewald, M. A. Kraft, S. P. Culver, A. Senyshyn, W. G. Zeier, *Chem. Mater.* **2019**, *31*, 4936–4944.
- [42] Y. Zeng, B. Ouyang, J. Liu, Y.-W. Byeon, Z. Cai, L. J. Miara, Y. Wang, G. Ceder, *Science* **2022**, *378*, 1320–1324.
- [43] F. Strauss, J. Lin, M. Duffiet, K. Wang, T. Zinkevich, A.-L. Hansen, S. Indris, T. Brezesinski, *ACS Mater. Lett.* **2022**, *4*, 418–423.
- [44] F. Strauss, J. Lin, A. Kondrakov, T. Brezesinski, *Matter* **2023**, *6*, 1068–1070.
- [45] J. Lin, G. Cherkashinin, M. Schäfer, G. Melinte, S. Indris, A. Kondrakov, J. Janek, T. Brezesinski, F. Strauss, *ACS Mater. Lett.* **2022**, *4*, 2187–2194.
- [46] S.-K. Jung, H. Gwon, H. Kim, G. Yoon, D. Shin, J. Hong, C. Jung, J.-S. Kim, *Nat. Commun.* **2022**, *13*, 7638.
- [47] Y. Chen, T. Wang, H. Chen, W. H. Kan, W. Yin, Z. Song, C. Wang, J. Ma, W. Luo, Y. Huang, *Matter* **2023**, *6*, 1530–1541.
- [48] A. Behera, in *Advanced Materials An Introduction to Modern Materials Science* (Ed.: A. Behera), Springer International Publishing, Cham, **2022**, pp. 291–320.
- [49] C. Oses, C. Toher, S. Curtarolo, *Nat. Rev. Mater.* **2020**, *5*, 295–309.
- [50] R.-Z. Zhang, M. J. Reece, *J. Mater. Chem. A* **2019**, *7*, 22148–22162.
- [51] A. Sarkar, B. Breitung, H. Hahn, *Scr. Mater.* **2020**, *187*, 43–48.
- [52] C. M. Rost, E. Sachet, T. Borman, A. Moballegh, E. C. Dickey, D. Hou, J. L. Jones, S. Curtarolo, J.-P. Maria, *Nat. Commun.* **2015**, *6*, 8485.
- [53] J. Wang, Y. Cui, Q. Wang, K. Wang, X. Huang, D. Stenzel, A. Sarkar, R. Azmi, T. Bergfeldt, S. S. Bhattacharya, R. Kruk, H. Hahn, S. Schweidler, T. Brezesinski, B. Breitung, *Sci. Rep.* **2020**, *10*, 18430.
- [54] Y. Ma, Y. Ma, Q. Wang, S. Schweidler, M. Botros, T. Fu, H. Hahn, T. Brezesinski, B. Breitung, *Energy Environ. Sci.* **2021**, *14*, 2883–2905.
- [55] A. Sarkar, Q. Wang, A. Schiele, M. R. Chellali, S. S. Bhattacharya, D. Wang, T. Brezesinski, H. Hahn, L. Velasco, B. Breitung, *Adv. Mater.* **2019**, *31*, 1806236.
- [56] B. Yang, Y. Zhang, H. Pan, W. Si, Q. Zhang, Z. Shen, Y. Yu, S. Lan, F. Meng, Y. Liu, H. Huang, J. He, L. Gu, S. Zhang, L.-Q. Chen, J. Zhu, C.-W. Nan, Y.-H. Lin, *Nat. Mater.* **2022**, *21*, 1074–1080.
- [57] R. D. Shannon, *Acta Crystallogr. Sect. A* **1976**, *32*, 751–767.
- [58] A. Kuhn, O. Gerbig, C. Zhu, F. Falkenberg, J. Maier, B. V. Lotsch, *Phys. Chem. Chem. Phys.* **2014**, *16*, 14669–14674.
- [59] Y. Kato, S. Hori, T. Saito, K. Suzuki, M. Hirayama, A. Mitsui, M. Yonemura, H. Iba, R. Kanno, *Nat. Energy* **2016**, *1*, 16030.
- [60] H. Stöfler, T. Zinkevich, M. Yavuz, A.-L. Hansen, M. Knapp, J. Bednarčík, S. Randau, F. H. Richter, J. Janek, H. Ehrenberg, *J. Phys. Chem. C* **2019**, *123*, 10280–10290.
- [61] D. Bérardan, S. Franger, A. K. Meena, N. Dragoe, *J. Mater. Chem. A* **2016**, *4*, 9536–9541.
- [62] M. Gazda, T. Miruszewski, D. Jaworski, A. Mielewczyk-Gryń, W. Skubida, S. Wachowski, P. Winiarz, K. Dzierzgowski, M. Łapiński, I. Szpunar, E. Dzik, *ACS Mater. Lett.* **2020**, *2*, 1315–1321.
- [63] S. Muy, R. Schlem, Y. Shao-Horn, W. G. Zeier, *Adv. Energy Mater.* **2021**, *11*, 2002787.
- [64] J. Ding, PhD thesis, Duke University, **2022**.
- [65] A. Banerjee, X. Wang, C. Fang, E. A. Wu, Y. S. Meng, *Chem. Rev.* **2020**, *120*, 6878–6933.

Manuscript received: September 21, 2023

Accepted manuscript online: October 30, 2023

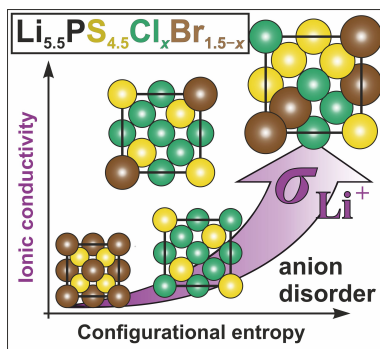
Version of record online: ■■■■■

Research Articles

All-solid-state Batteries

S. Li, J. Lin, M. Schaller, S. Indris, X. Zhang,
T. Brezesinski, C.-W. Nan, S. Wang,*
F. Strauss* [e202314155](#)

High-Entropy Lithium Argyrodite Solid Electrolytes Enabling Stable All-Solid-State Batteries



Configurational entropy (compositional disorder in the anion sublattice) shows a direct correlation with ionic conductivity in lithium argyrodite superionic solid electrolytes.